OPEN ACCESS
Saudi Journal of Engineering and Technology
Abbreviated Key Title: Saudi J Eng Technol
ISSN 2415-6272 (Print) | ISSN 2415-6264 (Online)
Scholars Middle East Publishers, Dubai, United Arab Emirates
Journal homepage: https://saudijournals.com

Original Research Article

How the Magnus Expansion Fails in Fermionic Systems: Breakdown Signatures in the Hubbard Model

Laraib-ul-Nissa[1]*, Waqar Yousaf[2], Taniyat Kanwal[3]

[1]School of Physics and Mechanics, Wuhan University of Technology, Wuhan, Hubei, China
[2]Hydrogen Technology, Campus Burghausen, Rosenheim Technical University of Applied Sciences (Rosenheim), 84489 Burghausen, Germany
[3]Department of Physics, Riphah International University, Islamabad, Pakistan

DOI: https://doi.org/10.36348/sjet.2026.v11i09.004 | **Received:** 27.06.2026 | **Accepted:** 20.08.2026 | **Published:** 14.09.2026

***Corresponding author:** Laraib-ul-Nissa
School of Physics and Mechanics, Wuhan University of Technology, Wuhan, Hubei, China

Abstract

The Magnus expansion is attractive for periodically driven quantum systems because every finite truncation exponentiates an anti-Hermitian generator and therefore preserves unitarity. Its practical failure in interacting fermionic systems is nevertheless subtle: a low-order approximation may remain unitary while becoming progressively less accurate as additional terms are retained. We establish order-resolved breakdown signatures for a half-filled, periodically driven one-dimensional Fermi-Hubbard chain. The one-period propagator is computed numerically exactly in the fixed-particle sector and compared with Magnus approximants through fourth order. Failure is defined operationally by a successive-order error ratio ($r_n=\varepsilon_n/\varepsilon_{n-1}\geq 1$), not by an unsupported claim of divergence of the infinite series. Across a raw (9×29) interaction-frequency grid ((U/J=0…,8), (ω/J=2…,16)), at least one added order loses improvement at 36.40% of the 261 sampled points. The smallest sampled frequency above which all retained orders improve throughout the remaining high-frequency tail rises from (ω/J=2.5) at (U=0) to (11.5) at (U/J=8). At (U/J=4), the highest (r_4=1) crossing occurs at (ω/J=7.719), followed by a monotone sampled tail from (ω/J=8). High-frequency error exponents approach the expected omitted-order scaling. A norm-based convergence certificate is consistently more conservative than the observed finite-order boundary. These results show that Magnus breakdown in the Hubbard model is order dependent, interaction shifted, and detectable before unitarity is lost.

Keywords: Magnus expansion, Floquet theory, Fermi-Hubbard model, periodically driven systems, exact diagonalization, convergence, prethermalization, fermions.

1. INTRODUCTION

Periodic driving provides a route to engineer effective tunnelling, artificial gauge fields, magnetic exchange, and correlated processes that are absent or difficult to isolate in static Hamiltonians. The formal foundation is Floquet theory: evolution over one period is represented by a time-independent generator, while micromotion describes dynamics within the period. In practice, that generator is rarely available in closed form. The Magnus expansion addresses this problem by expressing the propagator as the exponential of a series of time-ordered nested commutators [1,2]. Because the exponent of every consistent finite truncation remains anti-Hermitian for a Hermitian Hamiltonian, Magnus approximants are unitary at every retained order. This geometric advantage distinguishes them from direct truncations of the Dyson series [2].

Unitarity, however, is not an accuracy certificate. A finite Magnus approximation can be exactly unitary yet quantitatively poor. The distinction becomes decisive in interacting many-body systems, where the spectral width grows with system size, nested commutators generate increasingly nonlocal operators, and the thermodynamic-limit convergence radius can vanish even though optimally truncated high-frequency expansions accurately govern long prethermal windows [5-12]. Exact finite-dimensional convergence theorems provide useful sufficient conditions, including the norm bound $\int_0^T \|-iH(t)\|_2\, dt < \pi$, but failure of such a sufficient bound is not evidence of divergence [3,4]. Conversely, finite-order deterioration is a directly measurable numerical fact, but it does not alone establish the fate of the infinite series.

The Fermi-Hubbard model is a stringent setting for separating these statements. Its hopping and on-site interaction do not generally commute under a time-dependent Peierls phase. Repeated commutators therefore couple transport, occupation constraints, doublon-holon processes, and boundary effects. Near interaction-drive commensurabilities, effective descriptions can reorganize qualitatively: periodic Schrieffer-Wolff theory predicts different resonant and off-resonant Hamiltonians, while nonequilibrium dynamical mean-field theory and ultracold-atom experiments show interaction-sensitive prethermalization, doublon production, and energy absorption [13-18]. These observations motivate an error-based analysis of the expansion itself rather than an inference from heating or from a single observable.

Most discussions of Floquet-Magnus breakdown focus on asymptotic thermodynamic arguments, heating rates, or a comparison between an effective Hamiltonian and selected observables. Here we ask a narrower computational question: at a fixed point in parameter space, does adding the next Magnus term improve the complete one-period propagator? This produces an order-resolved criterion that can be evaluated without choosing an initial state or observable. It also exposes asymptotic behaviour: the best truncation order can change with frequency, and an order that fails at one point may recover at a higher frequency.

We apply this framework to a half-filled ($L=4$) open Fermi-Hubbard chain in the ($N\uparrow=N\downarrow=2$) sector. Exact one-cycle propagation and the first four Magnus terms are advanced jointly with an adaptive high-order solver. A frequency sweep at ($U/J=4$) is followed by a two-dimensional map over ($0\leq U/J\leq 8$) and ($2\leq \omega/J\leq 16$). Three complementary signatures are reported: the normalized propagator error (ε_n), the successive-order ratio (r_n), and the error-minimizing retained order (n^*). These are compared with the finite-sector norm certificate. Throughout, "failure" means an observed loss of improvement at a specified retained order; it is not used as a synonym for universal divergence.

2. Model and theoretical framework

2.1 Periodically driven Fermi-Hubbard chain

We consider spin-1/2 fermions on an open chain of (L) sites with a spatially uniform time-dependent Peierls phase. The particle-hole-symmetric Hamiltonian is

$$H(t) = -J\sum_{j=1}^{L-1}\sum_{\sigma=\uparrow,\downarrow}\left[e^{iA(t)}c_{j+1,\sigma}^{\dagger}c_{j,\sigma} + e^{-iA(t)}c_{j,\sigma}^{\dagger}c_{j+1,\sigma}\right] + U\sum_{j=1}^{L}\left(n_{j\uparrow}-\frac{1}{2}\right)\left(n_{j\downarrow}-\frac{1}{2}\right). \qquad (1)$$

Here $c^{\dagger}_{j\sigma}$ and $c_{j\sigma}$ create and annihilate a fermion of spin σ, $n_{j\sigma}=c^{\dagger}_{j\sigma}c_{j\sigma}$, J is the nearest-neighbour hopping energy, and $U\geq 0$ is the repulsive on-site interaction. The drive is

$$A(t) = K\sin(\omega t), \qquad T = \frac{2\pi}{\omega}, \qquad \hbar = J = 1. \qquad (2)$$

The amplitude is fixed at ($K=1$). Open boundaries remove the translational simplifications of a periodic chain and retain boundary-generated commutators even at ($U=0$). The calculations use ($L=4$) and half filling, ($N\uparrow=N\downarrow=2$).

2.2 Exact Floquet propagator

The exact one-period evolution operator at stroboscopic origin ($t_0=0$) is

$$U_F \equiv U(T,0) = \mathcal{T}\exp\left[-i\int_0^T H(t)\,dt\right], \qquad U_F^{\dagger}U_F = I. \qquad (3)$$

Although one can write ($U_F = \exp[-iH_F T]$), the logarithm is branch dependent because quasienergies are defined modulo (ω). We therefore compare propagators directly. This avoids branch-selection artefacts and tests the complete fixed-sector evolution rather than a small subset of matrix elements or observables.

2.3 Magnus representation and order-by-order recursion

The Magnus representation writes the same propagator as [1,2]

$$U_F = \exp[\Omega(T)], \qquad \Omega(T) = \sum_{m=1}^{\infty}\Omega_m(T), \qquad \Omega_m^{\dagger} = -\Omega_m. \qquad (4)$$

For numerical stability, the period is mapped to the dimensionless phase ($\theta=\omega t\in[0,2\pi]$), with generator

$$G(\theta)=-\frac{i}{\omega}H(\theta),\qquad \frac{dU}{d\theta}=G(\theta)U(\theta),\qquad U(0)=I. \qquad (5)$$

The inverse differential of the exponential gives the Magnus equation

$$\frac{d\Omega}{d\theta}=G-\frac{1}{2}[\Omega,G]+\frac{1}{12}[\Omega,[\Omega,G]]+\cdots,\qquad [X,Y]=XY-YX. \qquad (6)$$

Collecting equal formal orders yields the recursion actually integrated in this work:

$$\frac{d\Omega_1}{d\theta}=G. \qquad (7)$$

$$\frac{d\Omega_2}{d\theta}=-\frac{1}{2}[\Omega_1,G]. \qquad (8)$$

$$\frac{d\Omega_3}{d\theta}=-\frac{1}{2}[\Omega_2,G]+\frac{1}{12}[\Omega_1,[\Omega_1,G]]. \qquad (9)$$

$$\frac{d\Omega_4}{d\theta}=-\frac{1}{2}[\Omega_3,G]+\frac{1}{12}\big([\Omega_1,[\Omega_2,G]]+[\Omega_2,[\Omega_1,G]]\big). \qquad (10)$$

All ($\Omega_m(0)=0$). Equations (7)-(10) are equivalent to the corresponding time-ordered nested-commutator integrals, while avoiding direct four-dimensional quadrature at every parameter point. The fourth-order implementation was independently checked at the reference point against direct simplex quadrature and an explicit nested-commutator identity before the parameter sweeps.

2.4 Operational breakdown signatures

The order-(n) Magnus propagator is

$$U_M^{(n)}=\exp\left(\sum_{m=1}^{n}\Omega_m\right),\qquad n=1,2,3,4. \qquad (11)$$

With fixed-sector dimension (D), the normalized Frobenius error is

$$\epsilon_n=\frac{\left\|U_F-U_M^{(n)}\right\|_F}{\sqrt{D}}. \qquad (12)$$

Normalization by ($\sqrt{D}$) makes (ε_n) an average matrix-scale discrepancy and permits direct comparisons across orders at fixed (D). The successive-order improvement ratio is

$$r_n=\frac{\epsilon_n}{\epsilon_{n-1}},\qquad n=2,3,4. \qquad (13)$$

Thus ($r_n<1$) means that order (n) improves the propagator, whereas ($r_n\geq 1$) is a finite-order breakdown signature. The locally optimal retained order is

$$n_*=\underset{1\leq n\leq 4}{\operatorname{argmin}}\ \epsilon_n. \qquad (14)$$

For a fixed (U), the sampled monotone-tail onset is defined as

$$\omega_{\text{tail}}(U)=\min\{\omega_k:\ r_2(\omega_j),r_3(\omega_j),r_4(\omega_j)<1 \text{ for every } \omega_j\geq\omega_k\}. \qquad (15)$$

This is a property of the sampled grid, not a fitted phase boundary. Linear interpolation is used only to report crossings of ($r_n=1$) between adjacent raw frequency points.

2.5 Finite-sector convergence certificate

For the finite (36×36) representation, a sufficient condition for convergence of the Magnus series is [3,4]

$$\int_0^T\|-iH(t)\|_2\,dt<\pi. \qquad (16)$$

Using ($\theta=\omega t$), the corresponding threshold is

$$\omega>\omega_{\text{cert}}(U)\equiv\frac{1}{\pi}\int_0^{2\pi}\|H(\theta;U)\|_2\,d\theta. \qquad (17)$$

Equation (17) is evaluated by Gauss-Legendre quadrature. Its satisfaction guarantees convergence in this finite sector; its violation is inconclusive.

3. Numerical methods and validation

3.1 Fixed-particle fermionic basis

The calculation is restricted to the conserved (($N_\uparrow,N_\downarrow)=(2,2)$) sector. Its dimension is

$$D=\binom{L}{N_\uparrow}\binom{L}{N_\downarrow}=\binom{4}{2}^2=36. \qquad (18)$$

Fock states are represented independently for the two spin species, while hopping matrix elements are generated with fermionic occupation rules. The interaction diagonal takes only the values (-1,0,1) in the shifted convention of Equation (1). At ($U=K=0$), the numerical ground-state energy is (-4.472135954999578J), agreeing with the analytic open-chain result within (1.8×10^{-15}J).

3.2 Joint propagation of exact and Magnus equations

The exact propagator and ($\Omega_1,\ldots,\Omega_4$) were advanced in a single solve over ($\theta\in[0,2\pi]$). A DOP853 adaptive integrator was used with relative tolerance (2×10^{-10}), absolute tolerance (2×10^{-12}), and maximum step ($2\pi/64$). The shared integration nodes prevent spurious comparisons caused by independent time grids. Stricter reference calculations used relative tolerance (2×10^{-12}), absolute tolerance (2×10^{-14}), and maximum step ($2\pi/128$).

The primary interaction-frequency grid contains ($U/J=0,1,\ldots,8$) and ($\omega/J=2,2.5,\ldots,16$), giving 261 raw parameter points. A wider ($U/J=4$) sweep extends to ($\omega/J=20$) to test high-frequency scaling. No error-dependent sampling, smoothing, or interpolated heat-map field was applied.

3.3 Validation gates

The foundation calculations tested sector size, particle numbers, Hermiticity, the noninteracting ground-state energy, exact-propagator convergence, periodicity, zero-drive evolution, and normalization. The exact midpoint propagator displayed the expected second-order refinement ratio (4.000620), while its unitarity error was (3.34×10^{-14}). In the joint adaptive sweeps, the largest exact-propagator unitarity residual was (2.09×10^{-10}); the largest Magnus-propagator unitarity residual was (3.33×10^{-14}); and the maximum anti-Hermiticity residual of the retained Magnus terms was zero to stored precision.

Table 1: Model and numerical design

Item	Specification
Lattice	One-dimensional open chain, ($L=4$)
Filling	($N\uparrow=N\downarrow=2$)
Fixed-sector dimension	($D=36$)
Energy units	($\hbar=J=1$)
Interaction map	($U/J=0,1,\ldots,8$)
Frequency map	($\omega/J=2,2.5,\ldots,16$)
Extended frequency cut	($U/J=4$), ($\omega/J=2,\ldots,20$)
Drive	($A(t)=\sin(\omega t)$), ($K=1$), ($t_0=0$)
Retained Magnus orders	($n=1,2,3,4$)
Primary integrator	DOP853, rtol (2×10^{-10}), atol (2×10^{-12})
Map visualization	Raw sampled cells; no smoothing

Table 2: Principal validation results.

Validation quantity	Result	Interpretation
Static Hamiltonian Hermiticity residual	(0)	Exact within stored precision
($U=0$) ground-state energy error	(1.78×10^{-15})	Analytic benchmark reproduced
Exact-propagator refinement ratio	(4.000620)	Expected second-order convergence
Reference exact unitarity residual	(3.34×10^{-14})	PASS
Maximum map exact unitarity residual	(2.09×10^{-10})	Below (5×10^{-10}) gate
Maximum Magnus unitarity residual	(3.33×10^{-14})	Unitarity preserved at all retained orders
Maximum term anti-Hermiticity residual	(0)	PASS

4. RESULTS

4.1 Frequency-resolved loss and recovery of order improvement

Figure 1 resolves the expansion at ($U/J=4$). At low frequency the four error curves are not hierarchically ordered. The first-order approximation is optimal for ($2\le\omega/J\le4$), third order becomes optimal over the intermediate sampled interval beginning at ($\omega/J=4.5$), and fourth order becomes optimal from ($\omega/J=8$). This is the central practical meaning of failure: retaining more terms can worsen the complete propagator, even though every approximation remains unitary.

The ratios identify the responsible orders. The ($r_2=1$) crossing occurs at ($\omega/J=4.977$). The third-order ratio has two closely spaced crossings at (3.371) and (3.538), reflecting a narrow nonmonotonic feature. The most persistent loss is fourth order: (r_4) exceeds one across the low-to-intermediate-frequency region and crosses its final unity boundary at ($\omega/J=7.719$). The first sampled point after which all remaining frequencies satisfy ($r_2,r_3,r_4<1$) is therefore ($\omega/J=8$).

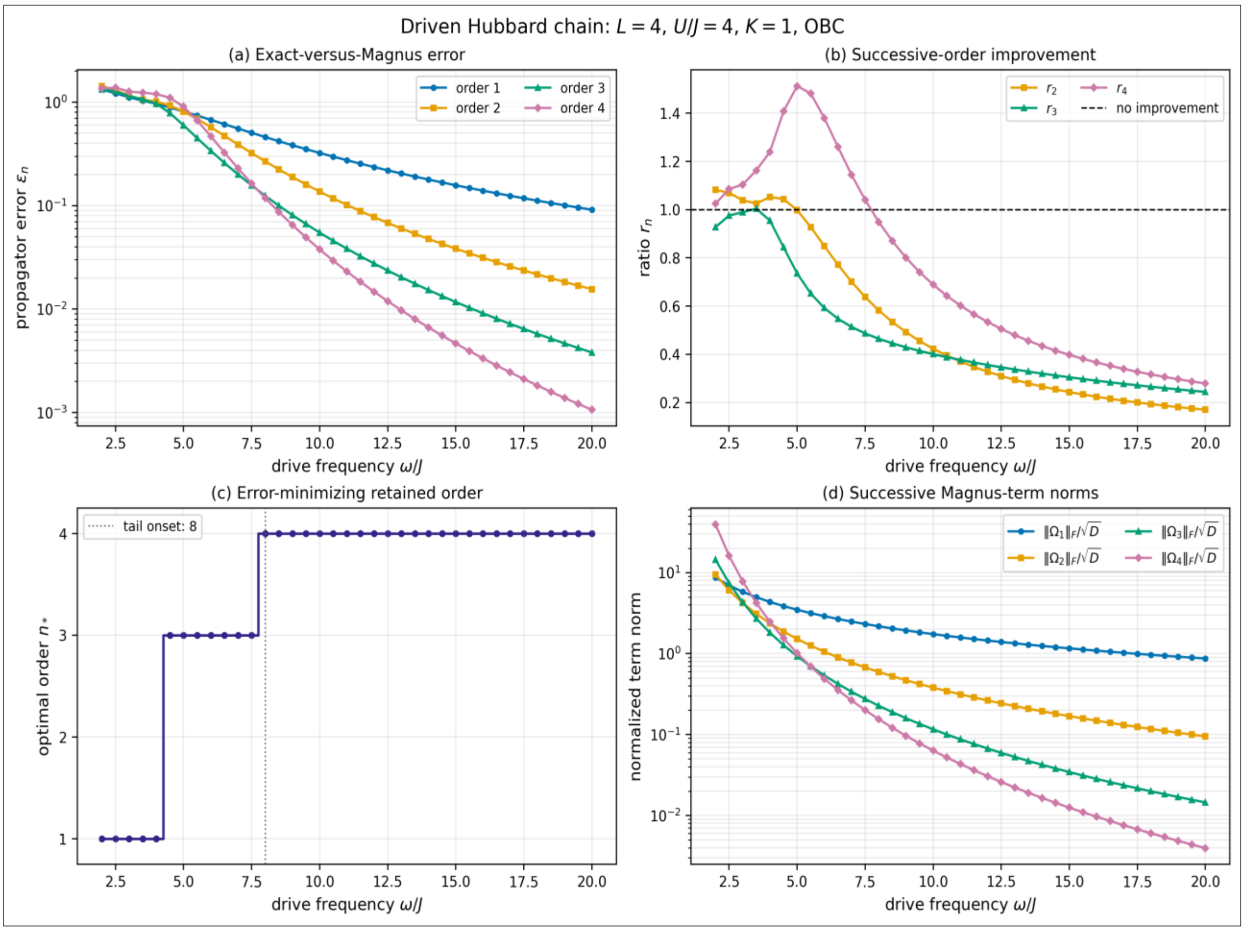

Figure 1: Order-resolved frequency sweep at (U/J=4)

(a) Normalized Frobenius error of the one-period propagator for Magnus orders 1-4. (b) Successive-order ratios; the dashed line marks (r_n=1). (c) Error-minimizing retained order (n); the dotted line marks the sampled monotone-tail onset. (d) Norms of the individual Magnus terms. Parameters: (L=4), (N↑=N↓=2), (K=1), open boundaries, and (J=ℏ=1). All markers are raw frequency samples.*

At the validated high-frequency reference point ((U/J,ω/J)=(4,10)), the errors decrease as

$$(\epsilon_1, \epsilon_2, \epsilon_3, \epsilon_4) = (0.322384,\ 0.136526,\ 0.054763,\ 0.037716). \qquad (19)$$

The corresponding ratios are ((r_2,r_3,r_4)=(0.423490,0.401116,0.688711)). Thus every added order improves the propagator, although the fourth-order gain is smaller than the second- and third-order gains. The term norms at this point decrease from (1.740731) to (0.379781), (0.116064), and (0.063305).

Table 3: Order-resolved quantities at (U/J=4) and (ω/J=10)

Order (n)	ϵ_n	r_n	$\|\Omega_n\|F/\sqrt{D}$
1	0.322384	-	1.740731
2	0.136526	0.423490	0.379781
3	0.054763	0.401116	0.116064
4	0.037716	0.688711	0.063305

At (ω/J≥12), log-log fits give error exponents (1.861), (3.139), (3.876), and (5.143) for orders 1-4, respectively. These approach the expected leading-omitted-term scaling

$$\epsilon_n(\omega) \propto \omega^{-(n+1)} \qquad (\omega \text{ large}). \qquad (20)$$

The agreement demonstrates that the recovered hierarchy is not merely a local crossing: it is connected continuously to the asymptotic high-frequency regime.

4.2 Interaction-frequency breakdown map

Figure 2 shows the same calculations performed for all 261 raw data samples. Fourth-order error falls sharply as a function of frequency but rises and forms shoulders as (U) increases. The map of the largest ratios clarifies the working boundaries. The black dots indicate where any of (r_2,r_3,r_4) exceed one. This occurs in 95 of the 261 cells, constituting the finite order loss ratio of

0.363985. On the other hand, the improved ratios occur in 166 cells, or 0.636015 of the total grid.

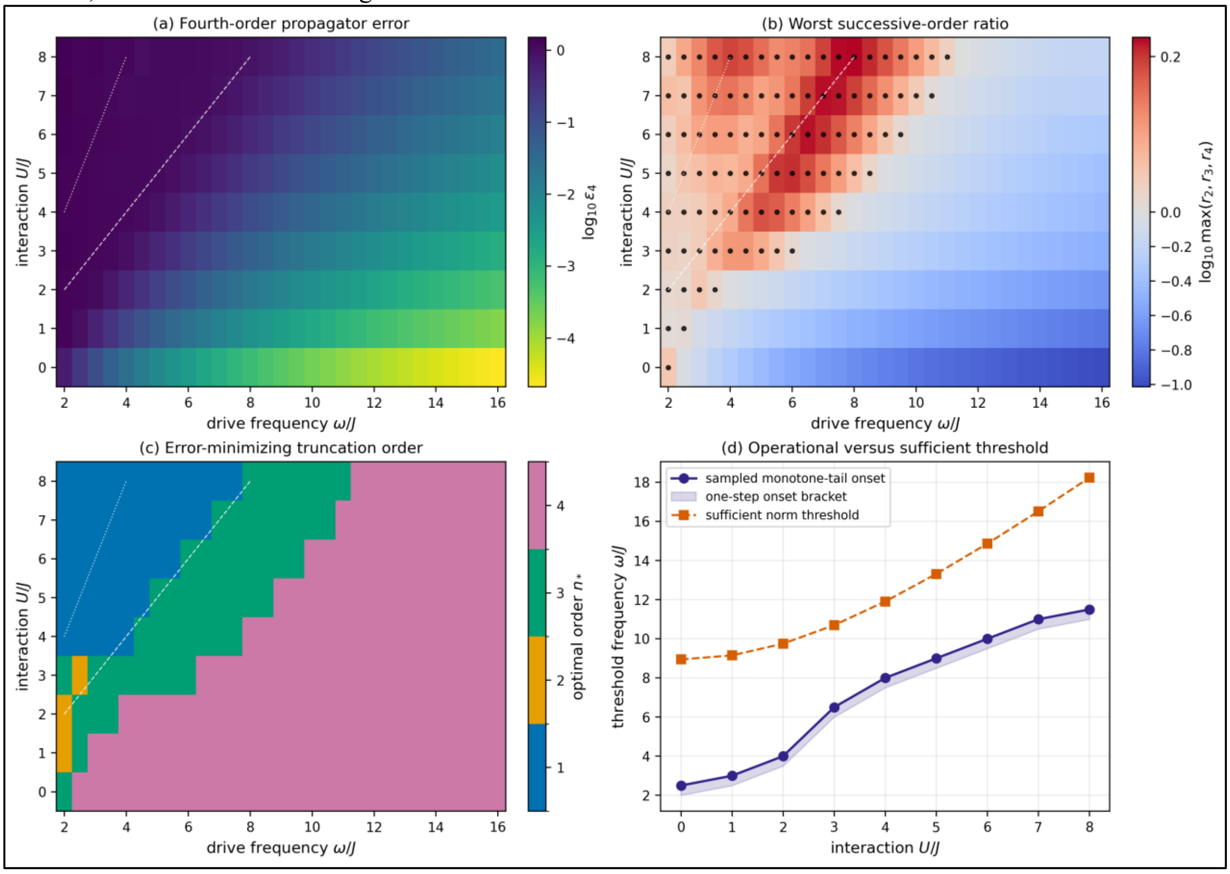

Figure 2: Interaction-frequency map of the breakdown signatures.

(a) ($\log_{10}\varepsilon_4$). (b) ($\log_{10}\max(r_2,r_3,r_4)$); black symbols indicate the raw cells with finite-order breakdown of improvement. (c) Optimal error-minimized order. (d) Monotone tail onset and its one-order lower bound compared against the sufficient norm criterion of Equation (17). The white dashed and dotted lines in Figures (a)-(c) correspond to (U=ω) and (U=2ω); these are commensurability guides, not fitted resonances. No interpolation or averaging was done here.

The optimal-order map shows all four of the retained orders: order 1 prevails in the low-frequency, strongly interacting regime; order 2 and 3 emerge in crossover regions; and order 4 holds sway in the high-frequency domain. The distribution rules out any possibility of having a universal cutoff that works for all of the orders. Instead, the empirical limit relies on the particular order being added, and the scale of the interaction.

The monotone tail onset increases systematically with (U): (2.5,3.0,4.0,6.5,8.0,9.0,10.0,11.0,) and (11.5) for (U/J=0,…,8). Likewise, the maximum fourth-order unity crossing moves upwards, from (2.321) when (U=0) to (11.482) when (U/J=8). The dependence deviates slightly from the linear behavior in the regime of small interaction due to the non-commutativity caused by open chain hopping, and to the possible multiple unity crossings at different ratios.

Table 4: Interaction dependence of the recovered high-frequency hierarchy

(U/J)	Lower sampled bracket	(ω_tail/J)	Highest (r_4=1) crossing	(ω_cert/J)
0	2.0	2.5	2.321	8.944
1	2.5	3.0	2.582	9.151
2	3.5	4.0	3.804	9.752
3	6.0	6.5	6.183	10.695
4	7.5	8.0	7.719	11.906
5	8.5	9.0	8.799	13.315
6	9.5	10.0	9.727	14.864
7	10.5	11.0	10.609	16.513
8	11.0	11.5	11.482	18.234

4.3 Selected interaction cuts and nonmonotonic structure

Figure 3 compares the cases (U/J=0), 4, and 8. At (U=0), the expected hierarchy is restored quickly, with only the fourth-order approximation failing at the lowest frequency. At (U/J=4), both (r_2)and (r_4)exceed unity over parts of the low-frequency range. By (U/J=8), the error curves become strongly nonmonotonic and the ratio structure is considerably more complex: (r_2) remains above unity across a broad frequency band, (r_3)crosses unity several times, and (r_4)does not fall below unity until approximately (ω/J≈11.5).

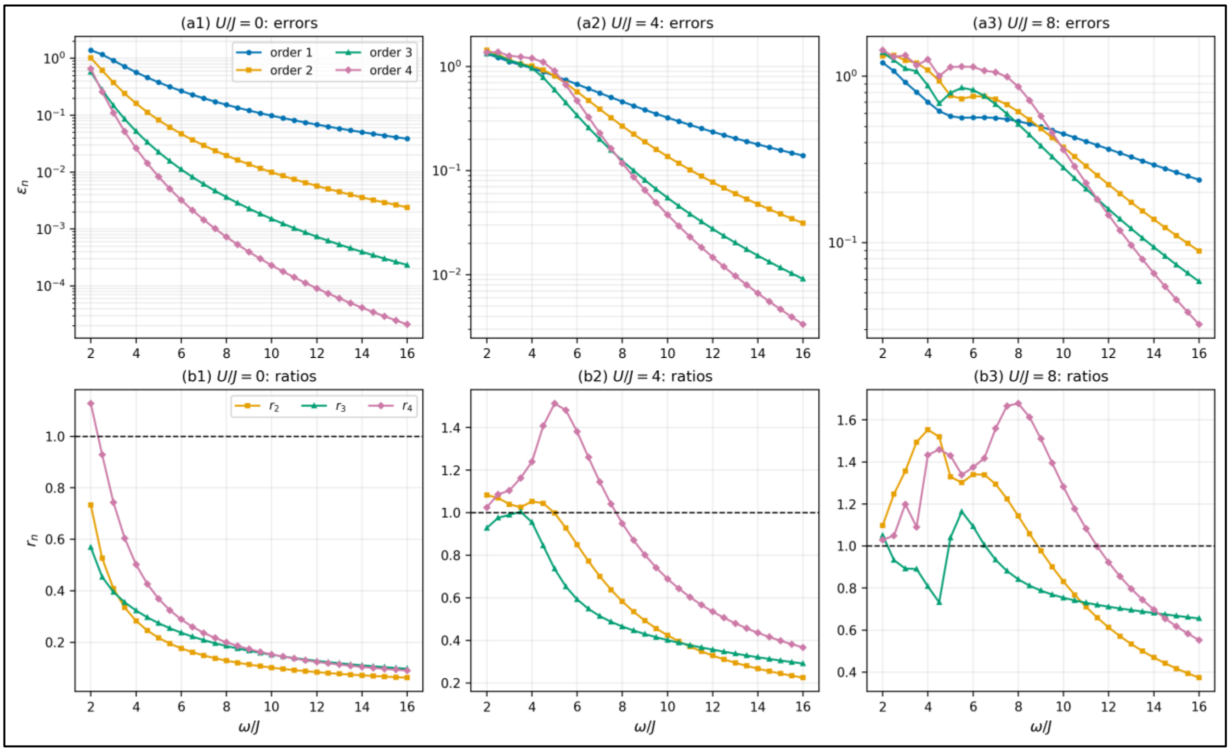

Figure 3: Selected interaction cuts

Top row: ($\varepsilon_1,\ldots,\varepsilon_4$) for (U/J=0,4,8). Bottom row: (r_2,r_3,r_4) with the no-improvement level (r_n=1). From the raw cut plots, it can be seen that more prominent interaction-driven shift and widening of the finite-order-loss region, and possibly more than one crossing of the latter instead of one boundary, occurs.

These features appear around frequencies similar to (U) and its fractions, yet our current finite-map description cannot give grounds to interpret each feature as resonance. Interaction-driven commensurabilities have been shown in driven-Hubbard theory to reorder the doublon-holon interactions and effective exchange [13-15].

Experiments and non-equilibrium dynamical mean-field computations confirmed increased absorption or double occupancy at resonant conditions [16-18]. Our map is compatible with an interpretation of interaction-driven competition, although (U=ω) and (U=2ω) are plotted as such purely for reference.

4.4 The norm certificate is sufficient but conservative

The finite-sector certificate for Equation (17) increases from (ω/J>8.944) at (U=0) to (>18.234) at (U/J=8). The certificate remains greater than the empirical sampled point where the interaction begins for each coupling strength. For (U/J≥7), the certificate remains unattainable even though all retained orders show improvement in a high-frequency tail within the range.

This difference is justified since the norm criterion uniformly bounds the entire infinite series and does not use any cancellations, symmetry, or the particular nature of the one-cycle propagator [3,4]. In comparison, (r_n) considers only the first four terms at specific points. The two criteria, hence, address different issues. The finite-order improvement, on the other hand, shows the validity of truncation at the selected points.

5. DISCUSSION

5.1 What "failure" means in this study

These findings distinguish three concepts that are often treated as equivalent. First, a truncation may be inaccurate, as indicated by a large (ε_n)Second, it may lose its asymptotic ordering when (r_n≥1). Third, the full infinite Magnus series may diverge. The present calculations establish only the first two. Maintaining this distinction is important because the finite (D=36) propagator always exists, and every retained Magnus approximation remains unitary even when its accuracy is poor.

Among the available diagnostics, (r_n)provides the clearest practical signal. An acceptable absolute error depends on the application, whereas ($r_n \geq 1$) directly shows that adding another order has made the approximation worse. The optimal-order map offers a complementary selection rule. In the low-frequency regime, truncating at first order can be more accurate than retaining all calculated terms. Above the interaction-dependent onset of the high-frequency tail, however, fourth order is consistently the most accurate of the truncations examined.

5.2 Connection to Floquet heating and prethermalization

High-frequency driving may yield a long-lived prethermal regime described by an optimally truncated effective Hamiltonian, even if the formal series expansion is divergent in the thermodynamic limit [8-12]. The recovery of ($r_n<1$) and the high-frequency power laws represent the finite-sector, single-period analog of that regime. While neither corresponds to a heating time per se, each marks the point at which the short-time generator becomes increasingly amenable to improvement.

In contrast, at lower frequencies, the series expansion faces competition from resonant multi-particle processes. In the Hubbard model, for instance, hopping changes the local doublon occupation and requires the expense of an interaction energy (U). A periodic drive can provide integer multiples of (ω) to allow resonant shifts of the exchange that enable doublon-holon binding or unbinding [13]. Non-equilibrium calculations indicate that resonant thermalization can occur with the failure of periodic Schrieffer-Wolff transformations [15], whereas experiments find long-lived driven states and near resonant absorption depending on the procedure and lattice structure [16-18]. Here, the interaction shifted error bands reveal the exact competition.

5.3 Why preserved unitarity can be misleading

The largest Magnus-unitarity residual remains at the (10^{-14})level throughout the map, including at points where ($r_n>1$). Unitarity by itself therefore does not reveal the loss of accuracy. This is an inherent feature of Magnus truncation rather than a numerical anomaly: exponentiating an anti-Hermitian partial sum necessarily produces a unitary matrix. A validation procedure based only on norm conservation may therefore accept an approximation whose full propagator error increases as additional orders are retained.

The comparison with the exact-propagator residual is equally revealing. Adaptive exact propagation produces a larger numerical unitarity residual, reaching (2.09×10^{-10}),yet it remains the reference solution because its accuracy is controlled through solver refinement. The Magnus propagators appear more unitary while being less accurate. Accuracy must therefore be established against a converged reference solution or an independent error bound, rather than inferred from unitary structure alone.

5.4 Scope and finite-size limitations

Such a calculation has been deliberately exhaustive over a small, fixed-size sector. This allows for direct storage and comparison of complete (36×36) propagators and for the stable calculation of up to fourth order. It does not demonstrate a thermodynamic limit transition, a universal resonance condition, or a converging radius independent of system size. Open boundary conditions also preserve the commutators that would otherwise be different under periodic boundary conditions.

A stronger test than this would be one involving a size series at fixed filling, utilizing matrix-free Krylov propagation and error estimators for local or typical states. In such a case, observables like double occupancy, energy absorption, and spectral statistics could all be compared against the operator error. Higher-order calculations must be performed in an asymptotic series, since the optimal order for minimizing error might grow in frequency before flipping over.

6. CONCLUSIONS

In the example study below, we will see how Magnus expansion becomes operationally inconsistent in a driven fermionic Hubbard model. The inconsistency does not lie in losing unitarity. The loss is in lack of systematic convergence, since in 36.40% of the sample points in the interaction-frequency plane, an extra included order in the Magnus expansion worsens the one-period propagator error relative to that of exact theory. This means that there exists an optimal truncation order depending on parameters. In particular, at ($U/J=4$), fourth order stops degrading at a crossing ($r_4=1$) occurring at ($\omega/J=7.719$), and then all included orders become better from ($\omega/J=8$) to the end of our sampled tail. Over ($U/J=0,\ldots,8$), the point where the tail starts shifts from (2.5) to (11.5). Thus, interaction systematically tightens the window of reliable low-order Floquet-Magnus theory.

The asymptotic errors at high frequency again show proper order-dependent scaling, so we can be sure that the identified boundary corresponds to an asymptotically controlled regime. Finite-sector norm certification stays much more conservative, underscoring that good error bounds and good empirical performance are not the same thing. Therefore, our precise conclusion is as follows: in the Hubbard model, Magnus inconsistency is order dependent, interaction dependent, and unitarity tests cannot catch it.

Data and Code Availability

The analysis produces the complete raw interaction-frequency table, the extended (U/J=4) frequency sweep, derived ratios and optimal orders, validation metadata, and publication figures. The map contains raw sampled cells without smoothing. The numerical workflow uses Python, NumPy, SciPy, and Matplotlib; all model parameters, solver tolerances, and diagnostic definitions required for reproduction are stated in the manuscript.

REFERENCES

1. Magnus, W. On the exponential solution of differential equations for a linear operator. *Communications on Pure and Applied Mathematics* 7, 649-673 (1954). https://doi.org/10.1002/cpa.3160070404
2. Blanes, S., Casas, F., Oteo, J. A. & Ros, J. The Magnus expansion and some of its applications. *Physics Reports* 470, 151-238 (2009). https://doi.org/10.1016/j.physrep.2008.11.001
3. Moan, P. C. & Niesen, J. Convergence of the Magnus series. *Foundations of Computational Mathematics* 8, 291-301 (2008). https://doi.org/10.1007/s10208-007-9010-0
4. Casas, F. Sufficient conditions for the convergence of the Magnus expansion. *Journal of Physics A: Mathematical and Theoretical* 40, 15001-15017 (2007). https://arxiv.org/abs/0711.2381
5. Bukov, M., D'Alessio, L. & Polkovnikov, A. Universal high-frequency behavior of periodically driven systems: from dynamical stabilization to Floquet engineering. *Advances in Physics* 64, 139-226 (2015). https://doi.org/10.1080/00018732.2015.1055918
6. Eckardt, A. & Anisimovas, E. High-frequency approximation for periodically driven quantum systems from a Floquet-space perspective. *New Journal of Physics* 17, 093039 (2015). https://doi.org/10.1088/1367-2630/17/9/093039
7. D'Alessio, L. & Rigol, M. Long-time behavior of isolated periodically driven interacting lattice systems. *Physical Review X* 4, 041048 (2014). https://doi.org/10.1103/PhysRevX.4.041048
8. Kuwahara, T., Mori, T. & Saito, K. Floquet-Magnus theory and generic transient dynamics in periodically driven many-body quantum systems. *Annals of Physics* 367, 96-124 (2016). https://doi.org/10.1016/j.aop.2016.01.012
9. Abanin, D. A., De Roeck, W. & Huveneers, F. Exponentially slow heating in periodically driven many-body systems. *Physical Review Letters* 115, 256803 (2015). https://doi.org/10.1103/PhysRevLett.115.256803
10. Abanin, D. A., De Roeck, W., Ho, W. W. & Huveneers, F. Effective Hamiltonians, prethermalization, and slow energy absorption in periodically driven many-body systems. *Physical Review B* 95, 014112 (2017). https://doi.org/10.1103/PhysRevB.95.014112
11. Abanin, D. A., De Roeck, W., Ho, W. W. & Huveneers, F. A rigorous theory of many-body prethermalization for periodically driven and closed quantum systems. *Communications in Mathematical Physics* 354, 809-827 (2017). https://doi.org/10.1007/s00220-017-2930-x
12. Mori, T., Kuwahara, T. & Saito, K. Rigorous bound on energy absorption and generic relaxation in periodically driven quantum systems. *Physical Review Letters* 116, 120401 (2016). https://doi.org/10.1103/PhysRevLett.116.120401
13. Bukov, M., Kolodrubetz, M. & Polkovnikov, A. Schrieffer-Wolff transformation for periodically driven systems: strongly correlated systems with artificial gauge fields. *Physical Review Letters* 116, 125301 (2016). https://doi.org/10.1103/PhysRevLett.116.125301
14. Herrmann, A., Murakami, Y., Eckstein, M. & Werner, P. Floquet prethermalization in the resonantly driven Hubbard model. *EPL* 120, 57001 (2017). https://doi.org/10.1209/0295-5075/120/57001
15. Peronaci, F., Schiró, M. & Parcollet, O. Resonant thermalization of periodically driven strongly correlated electrons. *Physical Review Letters* 120, 197601 (2018). https://doi.org/10.1103/PhysRevLett.120.197601
16. Görg, F. *et al.,* Enhancement and sign change of magnetic correlations in a driven quantum many-body system. *Nature* 553, 481-485 (2018). https://doi.org/10.1038/nature25135
17. Messer, M. *et al.,* Floquet dynamics in driven Fermi-Hubbard systems. *Physical Review Letters* 121, 233603 (2018). https://doi.org/10.1103/PhysRevLett.121.233603
18. Sandholzer, K. *et al.,* Quantum simulation meets nonequilibrium dynamical mean-field theory: exploring the periodically driven, strongly correlated Fermi-Hubbard model. *Physical Review Letters* 123, 193602 (2019). https://doi.org/10.1103/PhysRevLett.123.193602
19. Haga, T. Divergence of the Floquet-Magnus expansion in a periodically driven one-body system with energy localization. *Physical Review E* 100, 062138 (2019). https://doi.org/10.1103/PhysRevE.100.062138
20. Ikeda, T. N. & Polkovnikov, A. Fermi's golden rule for heating in strongly driven Floquet systems. *Physical Review B* 104, 134308 (2021). https://doi.org/10.1103/PhysRevB.104.134308